47th AIAA Aerospace Sciences Meeting Including The New Horizons Forum and Aerospace Exposition
5 - 8 January 2009, Orlando, Florida

AIAA 2009-536

Fluid Dynamics of Pitching and Plunging Airfoils of Reynolds Number between 1×10^4 and 6×10^4

Chang-kwon Kang[1]*, Yeon Sik Baik[1]*, Luis Bernal[2]*, Michael V. Ol[3]**, and Wei Shyy[4]*

University of Michigan, Ann Arbor, MI 48109, U.S.A.

***U.S. Air Force Research Laboratory, Wright-Patterson Air Force Base, OH 45433, U.S.A.*

We consider a combined experimental (two-dimensional particle image velocimetry in a water tunnel) and computational (two-dimensional Reynolds-averaged Navier-Stokes) investigation to examine the effects of chord Reynolds number on the dynamics of rigid SD7003 airfoil undergoing pitching and plunging motion in nominally two-dimensional conditions. Appreciable qualitative distinction in a moderately dynamically-stalled case in going from $Re = 1\times10^4$ to $Re = 6\times10^4$ was observed, suggesting nontrivial impact of viscosity even in conditions of strong forcing by motion kinematics. Additionally, computed lift coefficient time history is compared with Theodorsen's unsteady linear airfoil theory. The velocity and vorticity fields were in excellent agreement between experiment and computation for those phases of motion where the flow was attached; moderate agreement was achieved when the flow was separated. The small disagreements were consistent with the expected inaccuracies due to the turbulence model used. Similarly, Theodorsen's theory was able to predict the computed lift coefficient quite well when the flow was attached, and moderately acceptable otherwise.

Nomenclature

A = pitch amplitude, in degrees
C_L = airfoil lift coefficient per unit span
c = airfoil chord (=152.4mm)
f = airfoil oscillation pitch/plunge frequency
ω = pitch/plunge circular frequency
h_0 = non-dimensional plunge amplitude
k = reduced frequency of pitch or plunge, $k = 2\pi fc/(2U_\infty)$
St = Strouhal number, $St = 2fh_0/U_\infty = 2kh_0/\pi$
U_∞ = free stream (reference) velocity
u_i = velocity vector in indicial notation
x_i = position vector in indicial notation
Re = Reynolds number, $Re = U_\infty c/\nu$, ν taken as 10^{-6} in SI units for water at 20℃
α = kinematic angle of incidence due to pitch
α_0 = mean angle of attack (that is, the constant pitch angle offset from zero)
α_e = total angle of attack from trigonometric combination of pitch and plunge
x_p = pitch pivot point: fraction of chord downstream from airfoil leading edge
h = plunge position as function of time
t/T = dimensionless time, in fractions of one oscillation period

[1] Graduate Research Assistant, University of Michigan, Department of Aerospace Engineering
[2] Associate Professor, University of Michigan, Department of Aerospace Engineering, lpb@umich.edu
[3] Aerospace Engineer, Air Vehicles Directorate, Wright-Patterson AFB, Michael.Ol@wpafb.af.mil
[4] Clarence L. "Kelly" Johnson Collegiate Professor and Chair, University of Michigan, Department of Aerospace Engineering, weishyy@umich.edu

ϕ = phase difference between pitching and plunging; positive → pitch leads
λ = ratio of pitch-amplitude to plunge-induced angle of attack

I. Introduction

The unsteady aerodynamics of biological flyers has been the subject of numerous investigations by biologists and aerodynamicists. The recent monograph by Shyy *et al.*[1] provides a detailed review of the subject. Important features of the aerodynamics of biological flyers are large motion amplitude, small size and low flight speeds. As size becomes smaller the Reynolds number decreases and the flow field becomes more unsteady. As a result, the interaction between the fluid and the wing kinematics becomes more complex, including phenomena such as formation of large scale vortex structures, onset of separation and reattachment, near-wall pressure and velocity variations, lag between the instantaneous wing orientation, three dimensional effects, and development of the corresponding flow field[2,3,4,5]. Many flyers in nature have high aspect ratio wings and flap at a Strouhal number in the range from 0.2 to 0.4[6], which suggests that fundamental features of vorticity dynamics and time-dependent aerodynamic loads must be accurately predicted. As reviewed by Shyy *et al.*[1] and reported by Tang *et al.*[7], Trizila *et al.*[8], for two-dimensional cases and Shyy and Liu[9] for three-dimensional cases, the fluid physics associated with the flapping wing is qualitatively and quantitatively influenced by the kinematics as well as the Reynolds number. These studies focus on the flow regime of the Reynolds number around 10^2 and 10^3, where the issues such as turbulence are less dominant. In this work, we focus on a higher Reynolds number regime, between 1×10^4 and 6×10^4.

Overall, the combination of low Reynolds number ($Re < 10^5$) phenomena and large topological changes in flow structure encountered in flapping wing flows suggest departure from classical unsteady airfoil theory[10]. Critical issues include the role of leading edge and trailing edge vortex shedding[11], interaction of the time dependent wing pressure distribution with shed vortices, and the role of transition in shear layers bounding regions of laminar separation. Prior to current interest in flapping wing aerodynamics, dynamic stall of helicopter blades was perhaps the main application for high-rate unsteady aerodynamics in a nominally two dimensional wing, but the Reynolds number is much higher. It was established that the dominant feature of dynamic stall is the formation and shedding of a strong vortex-like disturbance near the leading-edge. McCroskey *et al.*[12] pointed out that as the vortex passes over the airfoil surface, it significantly changes the chordwise pressure distribution and produces transient forces and moments that are fundamentally different from those in static stall. Comprehensive reviews of dynamic stall are given by McCroskey[13], Carr[14], and Carr and McCroskey[15]. Ohmi *et al.*[16,17] experimentally examined the starting flows past a two-dimensional oscillating and translating airfoil, finding that the reduced frequency is the dominant parameter of the flow. However, they also demonstrated that as the pitching frequency increases, the patterns of the vortex wake are dependent on both the reduced frequency and the amplitude. Visbal and Shang[18] performed numerical investigations of the flow structure around a rapidly pitching NACA0015 airfoil at Reynolds number of 10^4 by solving the full two-dimensional Navier-Stokes equations. They observed a strong dependence of the primary flow features on the pitch rate and pitch pivot point location. At a fixed axial location, the dynamic stall can be delayed with increased pitch rate, suggesting that lags between evolution of flow separation and the airfoil motion kinematics should increase with increasing reduced frequency. Choudhuri and Knight[19] examined the effects of compressibility, pitch rate, and Reynolds number on the initial stages of two-dimensional unsteady separation of laminar subsonic flow over a pitching airfoil in the Reynolds number ranging from 10^4 to 10^5, finding that increasing the Reynolds number hastens the appearance of the primary recirculating region.

The aforementioned studies focus mostly on transients following the initiation of the airfoil motion from rest. Others considered the periodic or phase-averaged behavior of pitch/plunge motions after initial transients have relaxed, typically with a focus on motion kinematics for optimal thrust efficiency. Platzer and Jones[20] discussed theoretical prediction of thrust efficiency compared with flow visualization and thrust measurements for an airfoil in pure-plunging motion over a range of reduced frequencies and reduced amplitudes. Young and Lai[21] used a two-dimensional Reynolds-Averaged Navier-Stokes (RANS) approach to study the frequency-amplitude parameter space for optimal thrust efficiency. Lian and Shyy[22] used RANS methods to study the effect of an abstraction of gusts on a pitching/plunging airfoil, with evidence that the flapping motion has gust load alleviation potential, and that gusts can cause hysteresis in the force history and affect the transition process.

In this paper, we study Reynolds number effects on the flow field of a nominally two-dimensional airfoil undergoing combined pitch- and plunge and pure plunge at Reynolds numbers 1×10^4, 3×10^4, and 6×10^4 is

presented. The two different sets of kinematics represent a weak dynamic stall and a stronger dynamic stall, respectively. Experimental and computational flowfield results are compared: phase-averaged Particle Image Velocimetry (PIV) measurements are reported, and two-dimensional RANS equations coupled with Menter's Shear Stress Transport (SST). In addition, lift coefficient computed using unsteady linear airfoil theory (Theodorsen[23]) is compared with the computed lift coefficient. The focus of the investigation is to qualitatively and quantitatively ascertain the role of two-dimensional effects such as leading edge vortex formation, vortex shedding, and phase lag between flow field and the instantaneous angle of attack, tracing the flowfield and lift coefficient time histories. Issues such as flow variations in the spanwise direction, leading-trailing edge vortex interaction with the wing as well as tip vortices are not addressed here; recent studies[4] provide insight into these topics. But as a secondary objective, favorable comparison between experiment and computation would suggest that three-dimensional effects would not be of primary importance in either, for the range of motions presently under consideration

II. Experimental and Computational Setup

A. Experimental Approach

1. Particle Image Velocimetry (PIV)

The PIV measurements were conducted in the 2-feet by 2-feet water channel facility at the University of Michigan. The water channel is capable of generating free stream velocity ranging from 5 cm/s to 40 cm/s and a turbulence intensity of approximately 1%. The PIV system includes a double-pulsed Nd-YAG laser (Spectra Physics PIV 300), light sheet formation optics, two dual frame digital cameras (Cooke Corp. PCO-4000), computer image acquisition system and control electronics. The airfoil motion is produced by a rotary stage (Velmex B4872TS Rotary Table) for the pitch motion , a linear traverse (Velmex 20-inch BiSlide) for the plunge motion, a linear traverse (Velmex 40-inch BiSlide) for the axial motion, and the associated computer control system (Velmex VXM-1-1 motor control). Figure 1 illustrates the experimental setup.

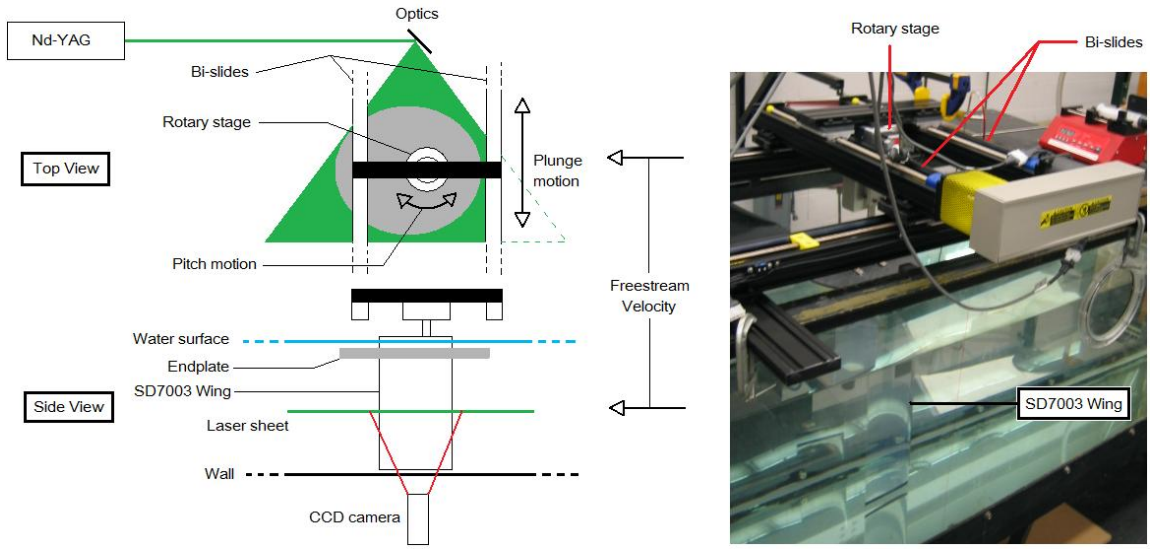

Figure 1. Schematics of PIV measurement setup (LEFT) and a photograph of water channel facility at the University of Michigan (RIGHT).

One aspect of how "3D effects" in a nominally 2D experiment is the intrusion of the model mounting scheme, the tunnel free-surface and blockage. It is desirable to compare alternative model mounting arrangements for the same nominal conditions. Airfoil pitch-plunge experiments of OI[24] had the airfoil mounted horizontally in the water tunnel test section, with vertical support rods in the test section center plane. The present arrangement reverts to the more common vertical cantilevered mounting of the airfoil, with the motion mechanism above the water line, and no part of the mounting mechanism below. To minimize free surface effects, an endplate was installed and just below the water surface.

The water channel was seeded with 3-μm diameter Titanium Dioxide particles. A small amount (8 drops) of a dispersant (DARVAN C-N, Vanderbilt) was used to produce a uniform distribution of particles and to help maintain the particles in suspension for long periods of time of the order of several days. The cameras were installed under the water channel test section and equipped with Nikon 105-mm Micro-Nikkor lenses to produce a magnification of 25 pixels/mm. With this magnification the time between exposures was adjusted to produce a nominal particle displacement of eight pixels at the free stream velocity in all cases. The PCO-4000 camera frame size is 4008 by 2672 pixels, which for the present magnification corresponds to 160 by 107 mm in the flow.

The airfoil tested in the present research is the SD7003 airfoil. The airfoil model was fabricated using stereo lithography and a transparent resin (DSM Somos 11122) to minimize laser reflection at the surface of the airfoil. The airfoil chord is 154 mm and spanned the entire depth of the water channel test section as shown in Figure 1. The distance between the airfoil model and the bottom surface of the test section was approximately 1 mm. An end-plate located below and as close as possible to the water surface was used during the experiments, and the laser sheet was positioned midway between the bottom wall and the water surface. The airfoil plunge motion was 154 mm. In order to capture the large amplitude motion and to avoid shadowing of the field of view, the PIV images were obtained in four separate tests for each flow condition. In two tests the airfoil leading edge region were imaged, and in the other two tests the airfoil trailing edge region were imaged. For the leading or trailing edge imaging experiments two tests were conducted, one capturing the extreme plunge motion locations (phases) with the two PCO-4000 cameras positioned side by side; and the other capturing the center locations of the plunge motion with only one camera. To ensure smooth image processing, the leading and trailing edge images contained an overlap region. The accuracy of the overlap region was directly linked to the accuracy of the traverse system. The accuracy of the axial Velmex BiSlide traverse is 0.00635 mm, which corresponds to approximately 1/6 of a pixel for the present magnification.

In the present measurements the velocity field at specific phases of the airfoil motion were recorded and used to calculate phase-averaged mean flow fields. The Nd-YAG laser, CCD cameras, rotary stage, and BiSlide were precisely synchronized to capture the desired phases of the motion. In a typical experiment 12 cycles of the motion were recorded and only the last 10 used to compute the phase averages. Each experiment was repeated 5 times for a total sample size of 50 images. Recording was initiated by the PIV system data acquisition, which triggered the airfoil motion controller. The PIV laser pulse period and the airfoil motion period were matched with an accuracy of 0.1 ms for a typical period of approximately 10 s. This produced a slight discrepancy in the airfoil position between the first image and the last image at phases with large speed of the airfoil motion. The maximum shift displacement for all cases was approximately 7 pixels, which corresponds to 0.28 millimeters. In terms of data processing, this discrepancy resulted in a datum point near the airfoil surface.

The PIV images were analyzed using an in-house developed MATLAB-based PIV analysis software. The particle displacement is determined in two passes using cross-correlation analysis of displaced interrogation windows. The location of the cross-correlation peak, which gives the particle displacement, is measured with sub-pixel resolution using a Gaussian fit of the cross correlation function around the peak. In the first low-resolution pass a fixed displacement of 20 pixels and an interrogation window of 64 × 64 pixel were used; in the second high-resolution pass the particle displacement measured in the first pass and an interrogation window size of 32 × 32 pixels were used. This corresponds to an approximate spatial resolution of the PIV measurements of ±0.64 mm. Several validation criteria were applied to the measured particle displacements. The peak magnitude must be at least three standard deviations above the mean of the cross-correlation function; and the displacement must be within a predetermined range of values in the x- and y-directions. The range of values in the first pass is fairly large to capture the large range of particle displacements found near the airfoil surface; and small (±5 pixels displacement) in the second pass. A median filter is used to find the particle displacement at the points where the PIV validation failed, and to remove outliers. A square grid with 8 pixel spacing was used for all the images. Near the surface of the airfoil, data points within 32 pixels from the boundary were discarded because the interrogation window would include pixels in the airfoil. This corresponds to four data points in the measurement grid.

2. Error Analysis

As noted earlier all phase-averaged results were computed by averaging the 50 images recorded at each phase of the motion. The corresponding 95% confidence interval for the phased-averaged values is ±29% of the standard deviation measured at each measurement point, which vary considerably depending on the flow

conditions and location in the flow. As expected, in the boundary layer near the wall the standard deviation was much larger than away from the walls. Also the standard deviation in the separated flow regions was significantly larger than in other parts of the flow. In terms of the free stream velocity, the 95% confidence interval is estimated as ±2.5% of the free stream velocity outside the separated flow regions and ±10% of the free stream velocity in the separated flow regions.

B. Computational Approach

The governing equations for the numerical simulation are the Reynolds-Averaged Navier-Stokes equations coupled with Menter's Shear Stress Transport (SST) model with the continuity equation for incompressible flow,

$$\frac{\partial}{\partial x_i}(u_i) = 0$$

$$\frac{\partial}{\partial t}(u_i) + \frac{\partial}{\partial x_j}(u_j u_i) = -\frac{1}{\rho}\frac{\partial p}{\partial x_i} + \frac{\partial}{\partial x_j}\left\{(\nu + \nu_t)\frac{\partial u_i}{\partial x_j}\right\}$$

$$\nu_t = \frac{a_1 k}{\max(a_1\omega, \|\nabla \times u_i\| F_2)}$$

$$\tau_{ij} = \rho\nu_t\left(\frac{\partial u_i}{\partial x_j} + \frac{\partial u_j}{\partial x_i}\right) - \frac{2}{3}\rho k\delta_{ij}$$

$$\frac{\partial k}{\partial t} + \frac{\partial}{\partial x_j}(u_j k) = -\frac{\tau_{ij}}{\rho}\frac{\partial u_i}{\partial x_j} - \beta^*\omega k + \frac{\partial}{\partial x_j}\left\{(\nu + \sigma_k\nu_t)\frac{\partial k}{\partial x_j}\right\}$$

$$\frac{\partial \omega}{\partial t} + \frac{\partial}{\partial x_j}(u_j \omega) = -\frac{\gamma}{\nu_t}\frac{\tau_{ij}}{\rho}\frac{\partial u_i}{\partial x_j} - \beta\omega^2 + \frac{\partial}{\partial x_j}\left\{(\nu + \sigma_\omega\nu_t)\frac{\partial \omega}{\partial x_j}\right\}$$

where a_1, β, β^*, γ, σ_k, σ_ω, F_2 are defined as in Menter's SST formulation[25], u_i is the velocity component in the i^{th} direction, x_i is the i^{th} component of the position vector, t is time, ρ is density, p is pressure, ν is the kinematic viscosity, and ν_t is the eddy viscosity. These equations were solved on two-dimensional grids with the in-house solver Loci-STREAM[26]. Loci-STREAM is a parallelized unstructured curvilinear pressure-based finite volume code with moving grid capabilities. The present calculations used implicit first order time stepping. The convection terms were treated using the second order upwind scheme[27,28] while pressure and

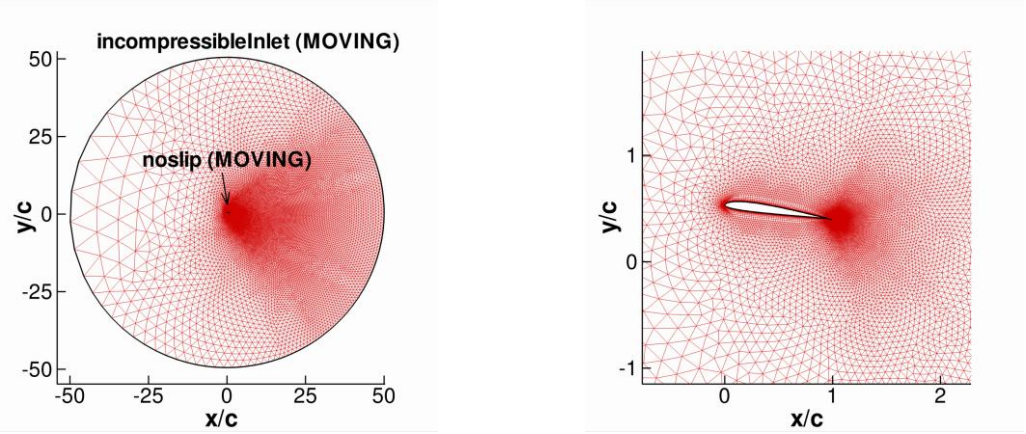

Figure 2. Unstructured grid in open bounded domain (LEFT) and its grid distribution near the airfoil (RIGHT) for oscillating SD7003 airfoil.

viscous terms were treated using second order schemes. The geometric conservation law[29,30], a necessary consideration in domains with moving boundaries, was satisfied.

The pitch- plunge and the pure plunge cases in open bounded domain were computed with Loci-STREAM on an unstructured grid with 46281 mixed elements, shown in Figure 2. The outer boundaries of the computational domain were 50 chord lengths apart. The boundary conditions are as follows: on the airfoil no-slip conditions were imposed; the outer boundaries were incompressible inlet. The computation was run assuming fully-turbulent, with no attempt to model transition or to prescribe the chordwise location of when to turn on the production term in the turbulence model.

C. Theodorsen's Unsteady Linear Airfoil Theory

One important issue in periodic oscillatory airfoil flows is the lag between the aerodynamic response and the airfoil motion kinematics. Quasi-steady models for lift coefficient have enjoyed some success even in high-frequency and geometrically-complex kinematics, such as the mechanical models of fruit-fly wings[31]. As a natural extension, constructing an explicit relation of the lag of putatively sinusoidal force response to sinusoidal motion kinematics, as a function of reduced frequency, amplitudes of pitch and plunge, phase difference between pitch and plunge, and the Reynolds number is necessary. This could then form a model for the lift response to more general motions and in more general configurations. Perhaps the simplest generalization beyond the quasi-steady approximation was obtained by Theodorsen model[23,32], for sinusoidal pitch-plunge of a thin airfoil, by assuming a planar wake and a trailing-edge Kutta condition, in incompressible inviscid flow. The lift coefficient time history is given by Eq. (1).

$$C_L(t) = 2\pi\big(1 - C(k)\big)\alpha_0 + \frac{\pi c}{2}\left\{\frac{\dot{\alpha}}{U_\infty} + \frac{\ddot{h}}{U_\infty^2} - \frac{c\big(2x_p - 1\big)\ddot{\alpha}}{2U_\infty^2}\right\} + 2\pi C(k)\left\{\frac{\dot{h}}{U_\infty} + \alpha + c\big(1.5 - 2x_p\big)\frac{\dot{\alpha}}{2U_\infty}\right\}. \tag{1}$$

The pitch and plunge motions are described by the complex exponentials, $\alpha(t) = \alpha_0 + A\mathrm{e}^{i\{2\pi(ft+\phi)\}}$ and $h(t) = h_0\mathrm{e}^{2\pi fti}$. The phase lead of pitch compared to plunge in terms of fractions of motion period is denoted by ϕ. In the most common case, motivated by considerations of maximum propulsive efficiency[33], pitch leads plunge by 90º, which results in ϕ = 0.25. The reduced frequency, k, is defined as $k = \pi fc/U_\infty = \pi St/(2h_0)$, and $C(k)$ is the complex-valued "Theodorsen function" with magnitude ≤ 1. It accounts for attenuation of lift amplitude and time-lag in lift response, from its real and imaginary parts, respectively. The first term is the steady-state lift and the second term is the "apparent mass" or noncirculatory lift due to acceleration effects. The third term models circulatory effects. Setting $C(k) = 1$ $(k = 0)$ recovers the quasi-steady thin airfoil solution. The noncirculatory term follows instantaneously the kinematics of motion, but evolution of the wake yields phase lag relative to the kinematics of airfoil motion in the circulatory term, which is predicted to peak for k approximately equal to 0.3.

The simplicity of Theodorsen's model is a powerful advantage when running large parameter studies, but its accuracy for separated flows with obviously nonplanar wakes remains an issue of contention. In this study we compare the Theodorsen's solution to the RANS computation for lift coefficient to address the model's applicability at $Re = O(10^4)$ for the reduced frequency of $k = 0.25$.

III. Results and Discussion

The motion kinematics time histories are described by

$$h(t) = h_0 c\cos(2\pi ft)$$
$$\alpha(t) = \alpha_0 + A\cos\{2\pi(ft + \phi)\}$$

where h is the location of the center of rotation of the airfoil measured normal to the free stream, h_0 is the normalized amplitude of the plunge motion, f is the motion physical frequency, c is the airfoil chord, α is the geometrical angle of attack measured relative to the incoming free stream with velocity, U_∞, α_0 is the mean angle of attack, and A is the amplitude of the pitch oscillation, see Figure 3.

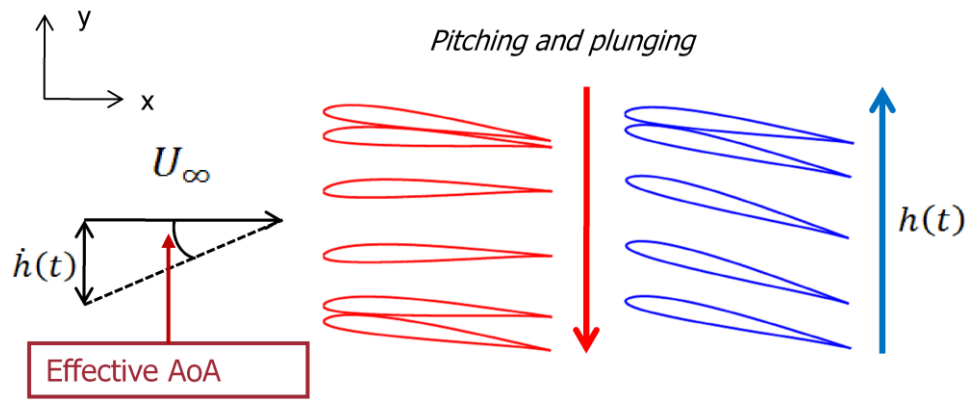

Figure 3. Schematic of SD7003 airfoil positions in downstroke (RED) and upstroke (BLUE), and the definition of the free stream direction and the effective angle of attack due to plunge motion.

The effective angle of attack, α_e, is the linear combination of pitch and plunge, and can be written as,

$$\alpha_e = \alpha_0 + \lambda \arctan(\pi St)\cos\{2\pi(ft+\phi)\} + \arctan\{\pi St \sin(2\pi ft)\}$$

where $St = 2fh_0/U_\infty$ is the Strouhal number, and $\lambda = A/\arctan\{\max(\dot{h})/U_\infty\}$ is the ratio of the maximum effective angles of attack of the pitch motion to the plunge motion, see Figure 4. The Reynolds number was varied by changing the flow speed, $Re = U_\infty c/\nu$. It is clear from the kinematics that maintaining the same effective angle of attack time history requires a constant Strouhal number and constant λ. Thus, as Re was varied the reduced frequency, $k = \pi fc/U_\infty = \pi St/(2h_0)$, and the Strouhal number were kept constant by varying the physical frequency proportionately.

The choice of reduced frequency, k = 0.25, was motivated in part by cruise-type conditions for flapping flight of bird. Although the corresponding Strouhal number, St = 0.08, is below the range for maximum propulsion efficiency[33], the present flow conditions are on the upper-end of the dynamic-stall literature, where the main application is helicopter blade aerodynamics[13,34], and for which the traditional analytical or phenomenological models in aeronautics tend to focus. As is often taken in applications motivated by maximizing propulsive efficiency of pitch-plunge[33], pitch leads plunge by one quarter of motion period: phase $\phi = 0.25$ and thus the airfoil "feathers", with the geometric pitch angle partially cancelling the plunge-induced angle of attack, $\arctan(\dot{h}/U_\infty)$. The amplitude of pitch, A, was computed from the value of λ= 0.6

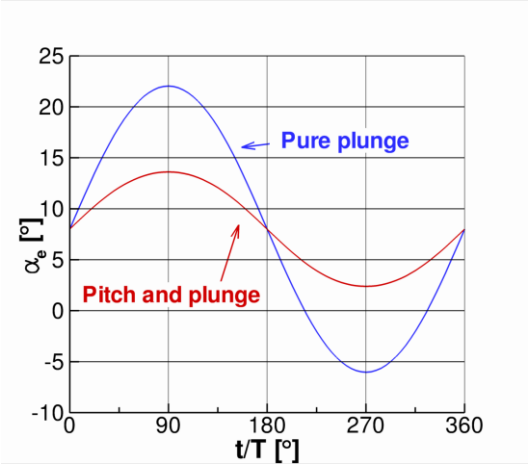

Figure 4. Time history of effective angle of attack for the pitching and plunging case and the pure plunging case.

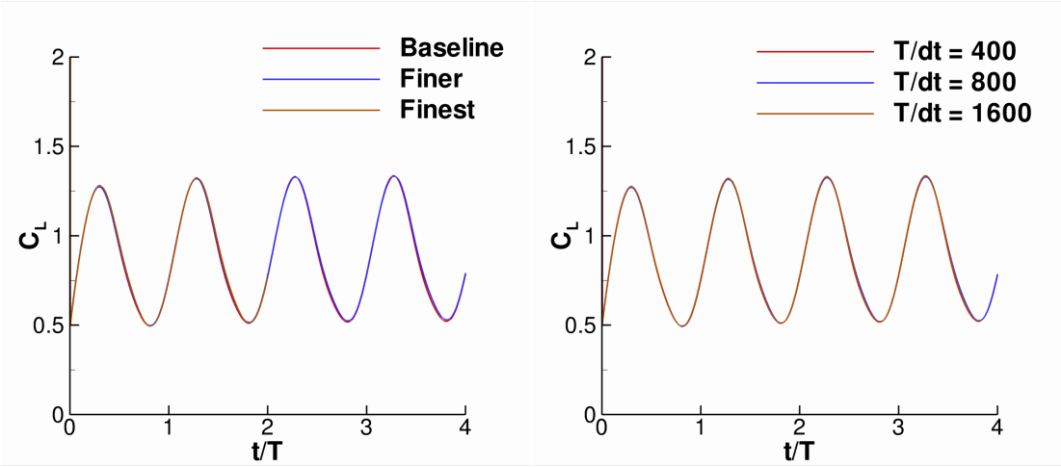

Figure 5. (LEFT) Time histories of the lift coefficients using the baseline (46281 cells), finer (119951 cells), and the finest (368099 cells) grid using T/dt = 400 over pitching and plunging SD7003 airfoil at Re = 6×10^4, k = 0.25, and λ = 0.6. (RIGHT)Time history of the lift coefficients using T/dt = 400, 800, and 1600 of a pitching and plunging SD7003 airfoil at Re = 6×10^4, k = 0.25, and λ = 0.6 on the baseline grid.

for the combined pitch-plunge case, while for the pure plunge case, λ =0. The total effective angle of attack time-trace, α_e, straddles the static stall value of approximately 11° [35]; this is just the sum of the pitch and plunge angles with appropriate phase shift.

A. Spatial and Temporal Sensitivity Study

Spatial and temporal sensitivity tests were performed for the pitch- and plunge case at Re = 6×10^4, k = 0.25, and λ = 0.6. To assess the grid sensitivity time histories of lift coefficient on the baseline (46281 cells), finer (119951 cells) and the finest (368099 cells) grids are compared in Figure 5 (LEFT) using a time step of T/dt = 400. All three solutions coincide, and thus all subsequent computations are performed on the baseline grid. To investigate temporal sensitivity, three time steps were used: T/dt = 400, 800, and 1600. Figure 5 (RIGHT) shows that the computations using T/dt = 400 on the grid with 46281 cells is sufficient to obtain grid and time step independent solution.

B. Global Flow Structures

1. Pitching and plunging case, Re = 6× 10^4

Figure 6 shows the normalized mean streamwise velocity, u_1, contours along with planar streamlines from the numerical and the experimental results for the motion-phases of 0°, 90°, 120°, 150°, 180°, 210°, and 270°. Overall, the agreement between the numerical computation and the experimental measurements is excellent, both in streamwise velocity contours as well as in flow structures. At Re = 6×10^4 the flow exhibits separation between the phases 90° to 210° shown from the experimental and numerical u_1 contours in Figure 6, corresponding to the maximum instantaneous effective angle of attack of 13.6°. Note that this value for the effective angle of attack is well beyond the static stall angle of 11°. At phase 0° the PIV measurements show slightly larger separation than the computational results; this will be discussed further in Section III.C.1.

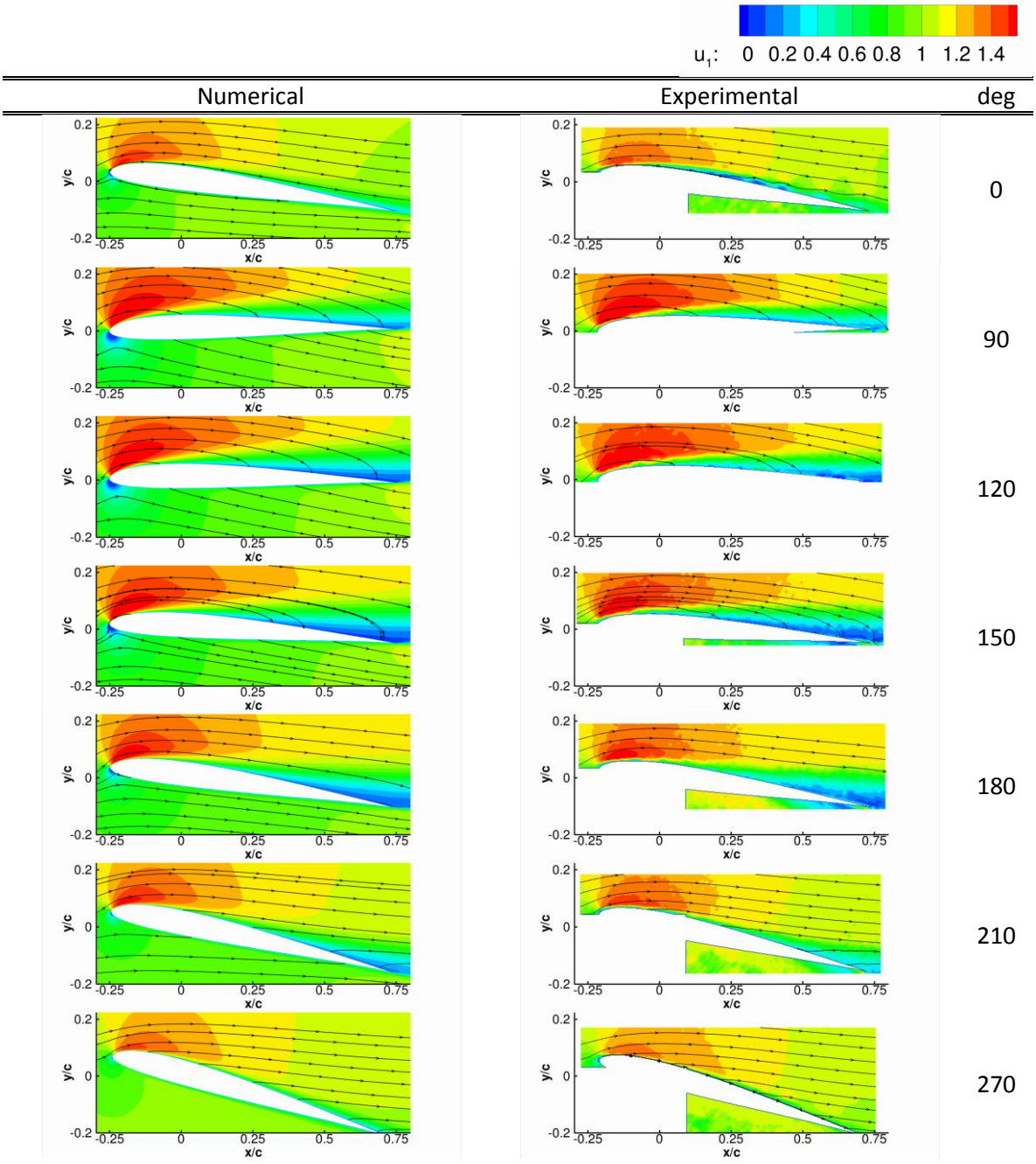

Figure 6. u_1 contours and the instantaneous streamlines over pitching and plunging SD7003 airfoil at k = 0.25, λ =0.6, and at Re = 6×10^4 from numerical and experimental results. The origin of the axes is translated to the pivot point at the quarter chord location of the airfoil.

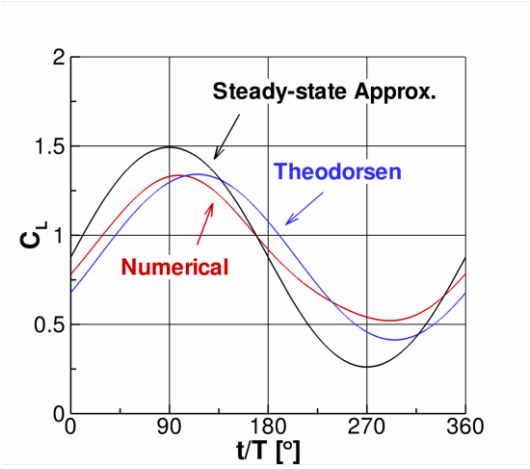

Figure 7. Time histories of lift coefficient for the pitching and plunging case (Re = 6×10^4, k = 0.25, λ = 0.6).

Lift coefficient time history is shown in Figure 7, comparing the quasi-steady ($2\pi\alpha_e$), Theodorsen, and computed values. Compared to the steady-state approximation, both Theodorsen's result and the computation show smaller lift amplitude as well as some phase lag indicating non-negligible influence from the wake via the circulatory terms in Eq. (1) at k = 0.25. Theodorsen's solution and numerical solution agree most closely at the phase 90°.At phase 180° the discrepancy is the largest, and hereboth numerical and experimental results show an open separation on the airfoil suction side (Figure 6). Since the Theodorsen's solution assumes a planar wake and Kutta condition at the trailing edge, the wake structure at phase 180° violates this condition causing the discrepancy in the lift coefficient. Overall, the Theodorsen's solution approximates the lift coefficient from the numerical computation better when the wake is 'planar'.

2. Pure plunging case, Re = 6× 10^4

Figure 8 shows the u_1 contour plots and the instantaneous streamlines from the numerical computation and the experimental measurements for the pure plunging SD7003 airfoil at the phases 0°, 90°, 120°, 150°, 180°, 210°, and 270°. The qualitative agreement between the two approaches is best when the flow is attached. PIV measurements show a thicker separated region on the suction side of the airfoil compared to the numerical prediction at phase 0°. At phase 90°, the experiment shows a closed separated region with apparent reattachment at *x/c* ~ 0.5; in contrast, the computation shows a thinner but open separation. The CFD and PIV comparison will be discussed more in detail in Section III.C.2

Figure 9 compares the lift coefficient computed from quasi-steady ($2\pi\alpha_e$), Theodorsen and CFD for the pure plunging case. Theodorsen's solution and the numerical result coincide for t/T = 0.75 to t/T = 0.25 while between t/T = 0.25 and t/T = 0.50, the numerical solution shows higher frequency behavior and deviates from the analytic prediction both in amplitude and phase. Similar to pitching and plunging case, the wake structures in both PIV and CFD results are not planar (see Figure 8), violating one of the assumptions for the Theodorsen's solution. The phase lag between the effective angle of attack and the response of the aerodynamic loading is smaller than in the pitching and plunging case, despite the larger extent of flow separation.

Unlike the pitching and plunging case where the flow showed only thin open separation, the pure plunging case generates large vortical structures at the leading edge between motion phases of 90° and 120°. Subsequently, this structure – which may be called a leading edge vortex – broadens, weakens, and convects downstream, eventually enveloping the entire airfoil suction side. By 180° phase of motion, reattachment is evinced at the leading edge, and sweeps downstream as the airfoil proceeds on the upstroke. The LEV and its subsequent development enhance suction, and thus also lift. This is seen in Figure 9 as a broad peak in lift at phase between 90° and 120° in the numerical lift coefficient result, followed by a drop in lift. The latter is associable with weakening and downstream convection of the LEV, and loss of leading-edge suction. Figure 10 shows the computed pressure coefficient contours, and normalized vorticity contours from both the numerical and the experimental results at the phase 90°.

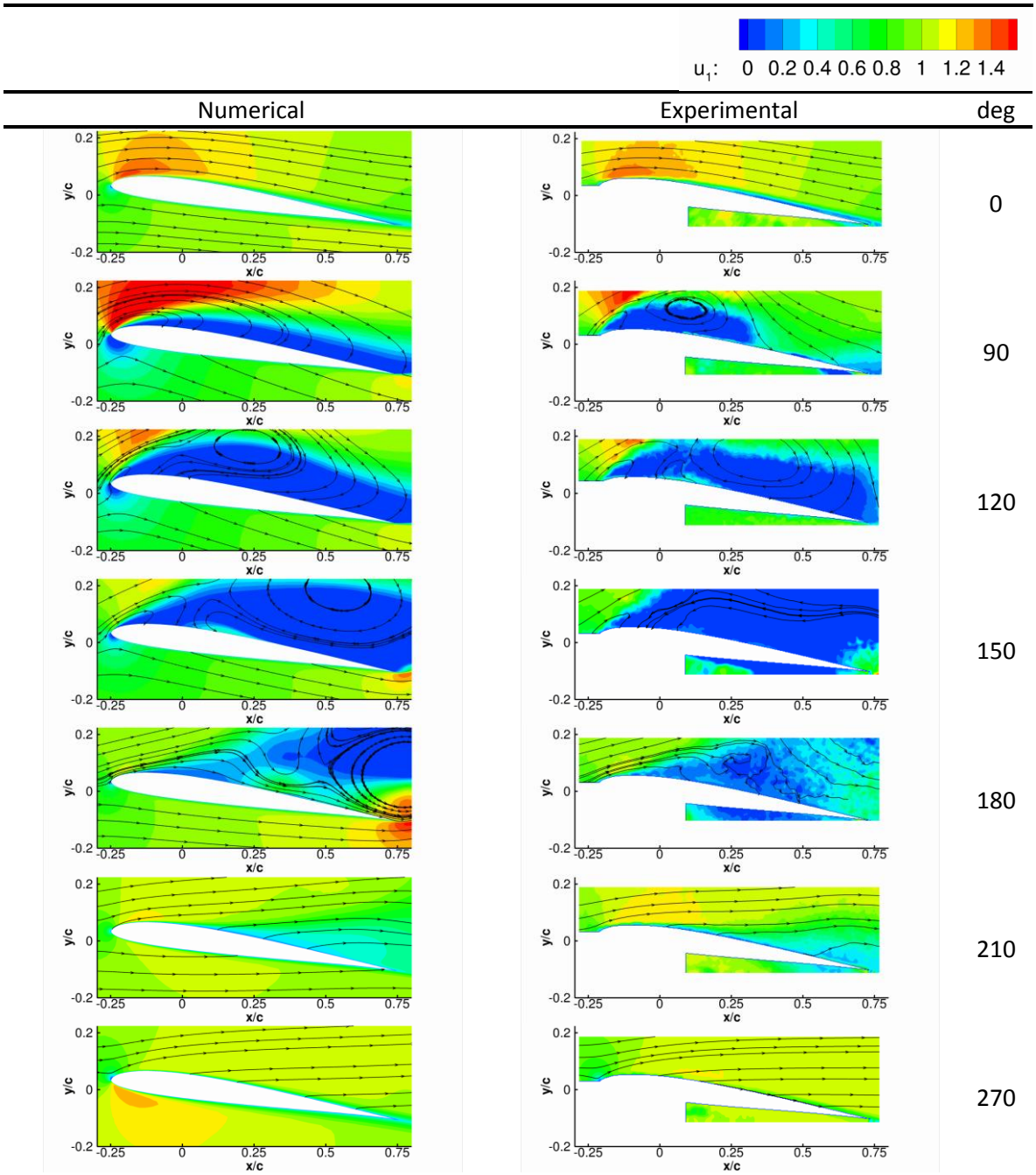

Figure 8. u_1 contours and instantaneous streamlines over pure plunging SD7003 airfoil at k = 0.25, λ =0.0, and at Re = 6×10^4 from numerical and experimental results. The origin of the axes is translated to the quarter chord location of the airfoil.

The LEV is notable in the experimental result, and to a lesser extent in the computation. At 180° the attenuation in vorticity peak values is consistent with the velocity contour plots and with the loss of suction near the leading edge, but there is a notable discrepancy between experiment and computation: the latter shows a strong trailing edge vortex, while the former does not. Most likely, this is the results of poor repeatability of the TEV from period to period, and thus its dissipation in the phase-averaged PIV results. Curiously, the experimental and the computational disagreements seem to be localized to the trailing edge,

whence it may be inferred that discrepancy in overall lift would be small in the integrated sense. This, however, would require substantiation when direct measurement of lift becomes available in the experiment.

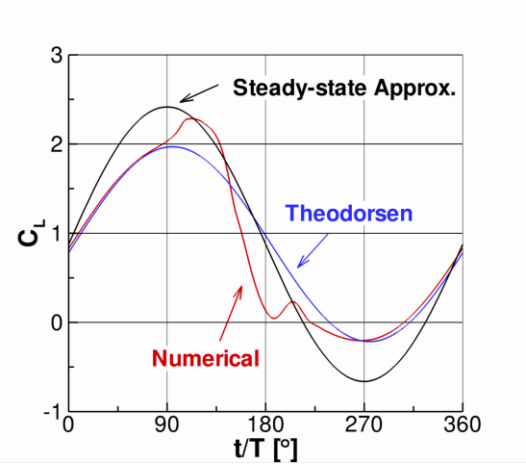

Figure 9. Time histories of lift coefficient for the pure plunge case (Re = 6×10^4, k = 0.25, λ=0.0).

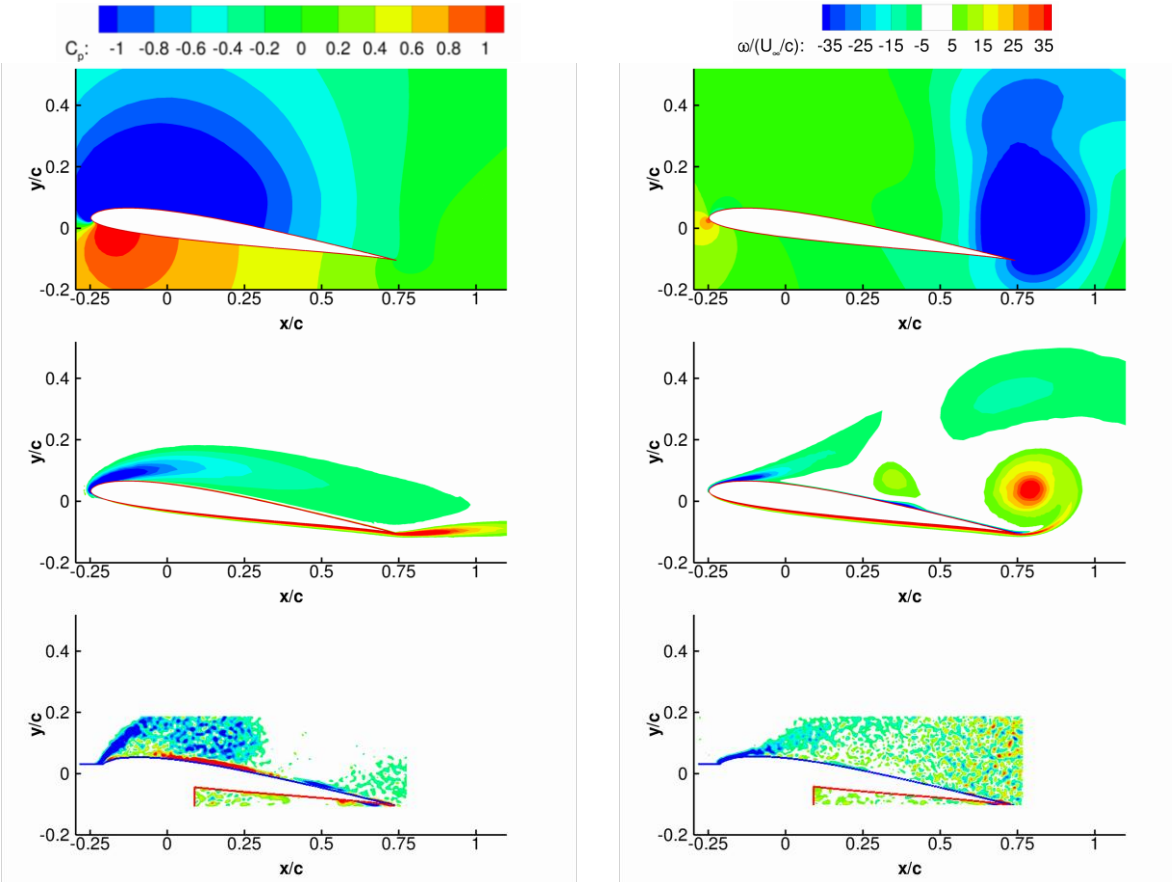

Figure 10. Pressure coefficient contours from the numerical computation (TOP), normalized vorticity contours from the numerical computation (MIDDLE), and normalized vorticity contours from the experimental measurements (BOTTOM) at the phases 90° (LEFT), and 180° (RIGHT) for the pure plunge case (Re = 6×10^4, k = 0.25, λ=0.0).

C. Reynolds Number Effect

1. Pitching and plunging case

The pitching and plunging case was conducted at three different Re: 1×10^4, 3×10^4 and 6×10^4, with best experimental-computational agreement better at $Re = 6\times10^4$. The agreement is illustrated in Figure 11, which shows u_1-component velocity profiles at 4 different phases located at $x/c = 0.25$.

Discrepancies between the experimental data and the numerical simulations were found at $Re = 1\times10^4$ and

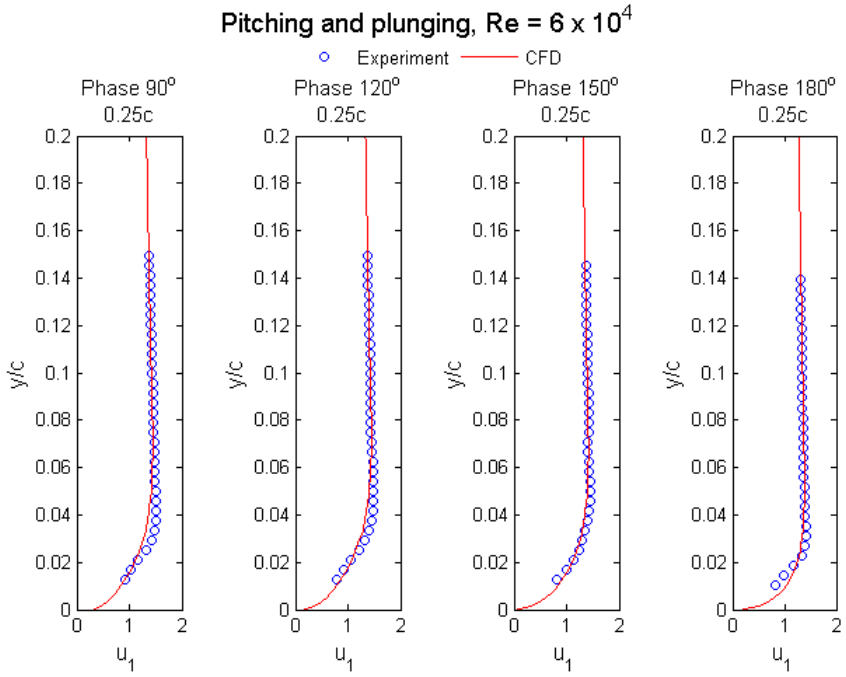

Figure 11. u_1 profiles from the CFD and PIV results at constant $x/c = 0.25$ at the phases 90°, 120°, 150° and 180° at $Re = 6\times10^4$ for the pitching and plunging case.

3×10^4. At $Re = 1\times10^4$, numerical simulation predicts a thin boundary layer throughout the length of the chord. Figure 12 plots u_1-component velocity profiles at two phases and two downstream locations as indicated.

The experimental data show reversed flow at the wall and a thicker boundary layer. This could indicate that the flow is laminar at the leading edge for $Re = 1\times10^4$. In the contour plots, a leading edge vortex is observed and this phenomenon only occurs at low Re. Far away from the airfoil surface, the experimental data is in good agreement with the numerical simulation results. This discrepancy could be explained by noticing that the SST turbulence model assumes that the flow is fully turbulent throughout the entire computational domain, thus promoting more prevalent flow attachment and delayed boundary layer separation.

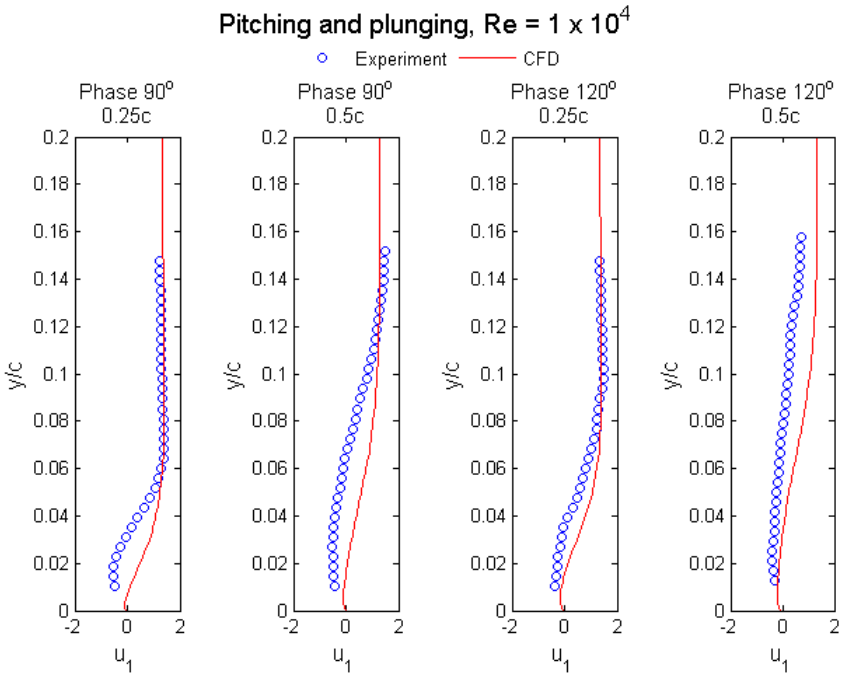

(a) u_1 profiles from the CFD and PIV results at constant $x/c = 0.25$, and 0.5 at the phases 90°, and 120°

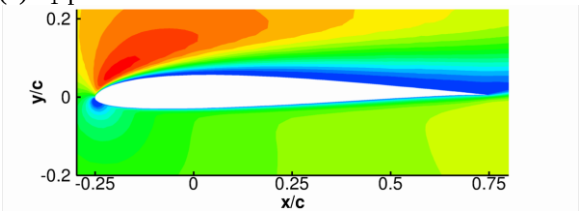

(b) u_1 contour at the phase 90°, CFD

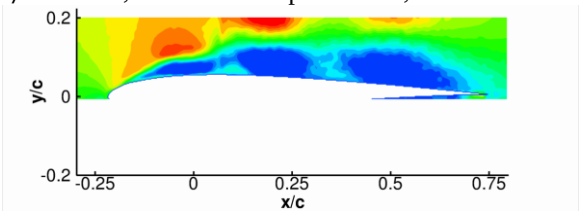

(c) u_1 contour at the phase 90°, PIV

Figure 12. u_1 profiles and contours from CFD and PIV results at Re = 1×10^4 for the pitching and plunging case.

At Re = 3×10^4, the agreement between the experiments and the numerical simulation was excellent except at phase 0° and 270°, where the numerical simulation under predicts flow separation near the trailing edge relative to the experimental data. The contour plots highlight the differences in the boundary thickness as the flow evolves downstream; the boundary layer from the numerical simulation is thinner compared to the experimental data. This observation is supported by Figure 13 which indicates that the flow is separated near the wall. The flow is not fully separated but the adverse pressure gradient is present which causes the flow to turn. On the other hand, numerical simulation predicts attached flow over the length of the airfoil. The reason behind this discrepancy can be explained by the same reasoning used for Re = 1×10^4 case; SST model assumes a turbulent flow over the entire flow region.

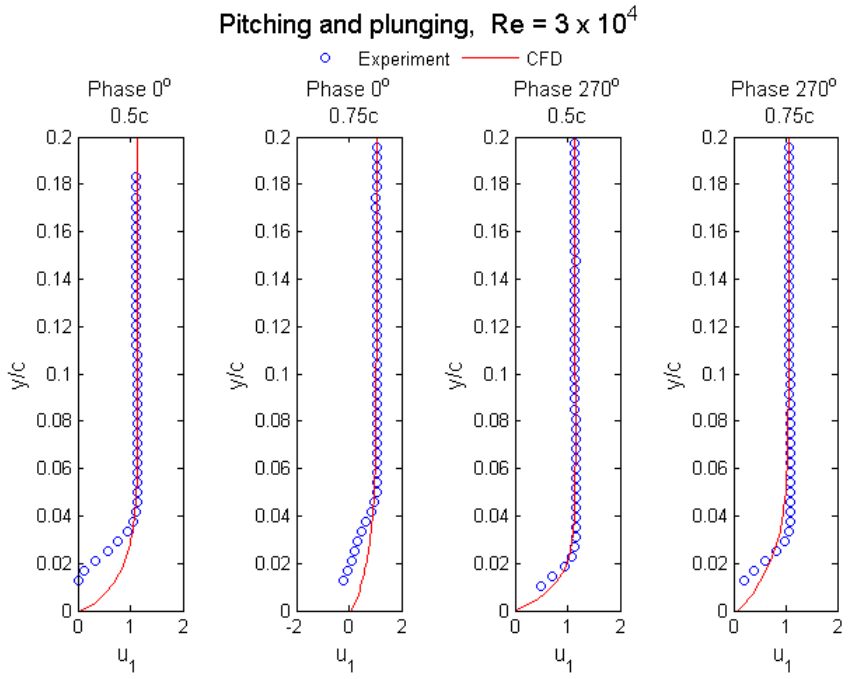

(a) u_1 profiles from the CFD and PIV results at constant $x/c = 0.5$ and 0.75 at the phases 0° and 270°

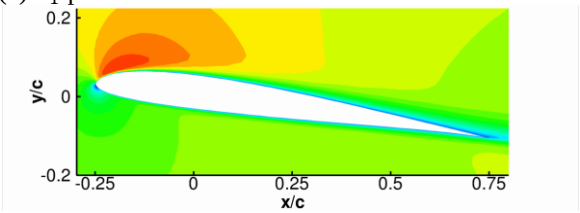

(b) u_1 contour at the phase 0°, CFD

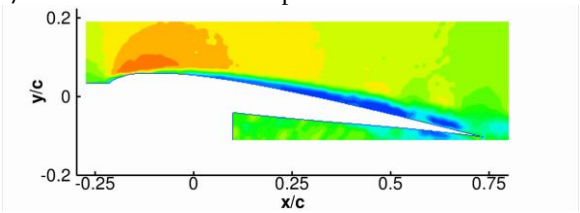

(c) u_1 contour at the phase 0°, PIV

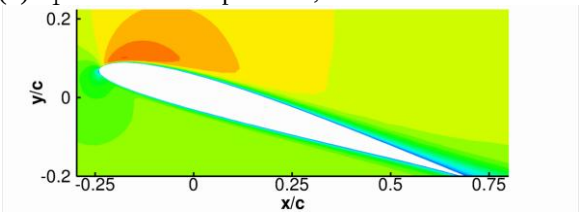

(d) u_1 contour at the phase 270°, CFD

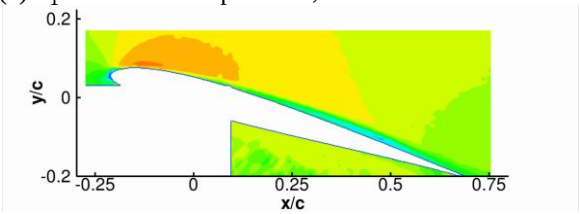

(e) u_1 contour at the phase 270°, PIV

Figure 13. u_1 profiles and contours from CFD and PIV results at Re = 3×10^4 for the pitching and plunging case.

2. Pure plunging case

Because of stronger separation and a more discernable LEV in the pure plunging case, one would expect the pure plunging case to evince larger regions of turbulent flow and less sensitivity to the assumptions about the flowfield turbulence in the computation. This creates an opportunity to verify the accuracy of the SST model used in the numerical simulation.

The pure plunging case was also considered at Re of 1×10^4, 3×10^4 and 6×10^4. In contradiction to pitching and plunging case, Re = 1×10^4 case produced the best agreement between experiment and computation while Re = 3×10^4 and 6×10^4 showed discrepancies but some interesting new insights. Figure 14 shows u_1-component velocity profiles from Re = 1×10^4 case.

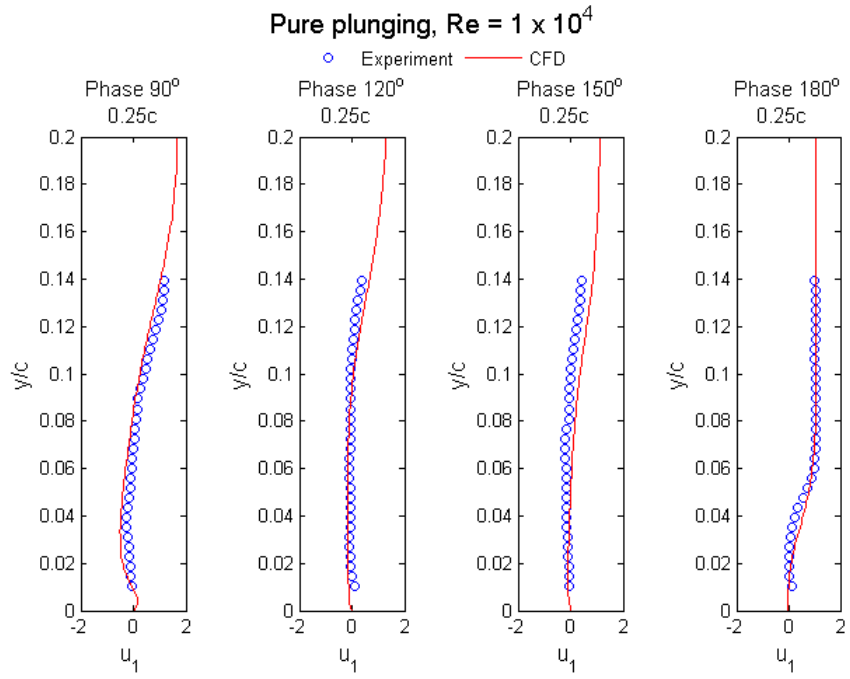

(a) u_1 profiles at constant $x/c = 0.25$ at the phases 90°, 120°, 150° and 180°

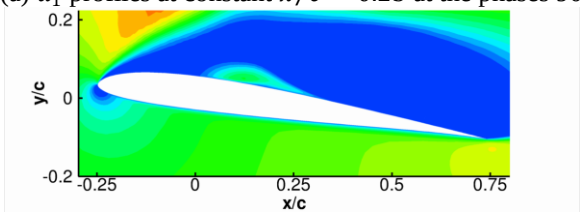

(b) u_1 contour at the phase 120°, CFD

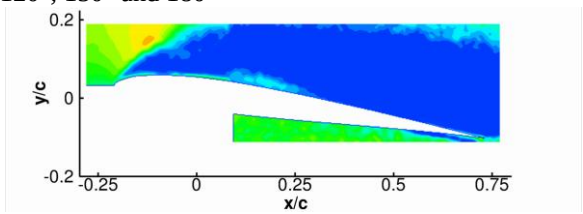

(c) u_1 contour at the phase 120°, PIV

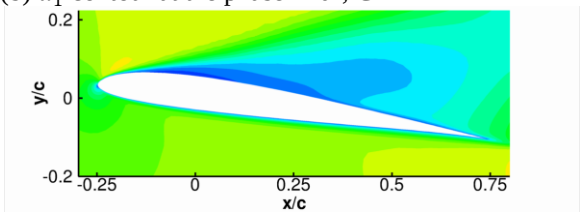

(d) u_1 contour at the phase 180°, CFD

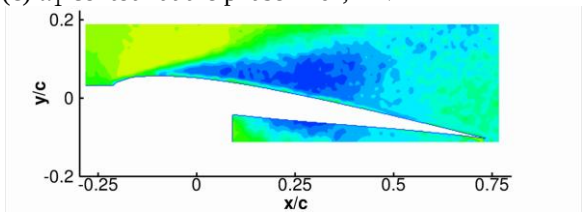

(e) u_1 contour at the phase 180°, PIV

Figure 14. u_1 profiles and contours from CFD and PIV results at Re = 1×10^4 for the pure plunging case.

Overall, the level of agreement between the experiments and the numerical simulation at Re = 1×10^4 is adequate. In Figure 14, the flow is separates at the leading edge and there is no sign of reattachment. The SST model captures the velocity profiles accurately for this particular case.

For Re = 3×10^4 and 6×10^4, it is observed from the contour plots that reattachment occurs at phase 90°. In order to capture the location of reattachment, the evolution of the velocity profiles in the downstream direction was analyzed.

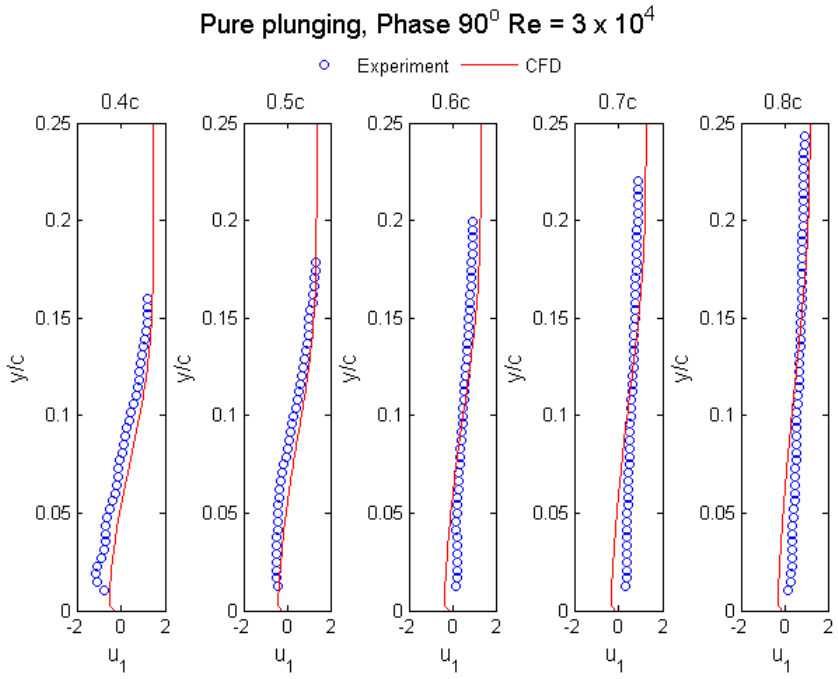

(a) u_1 profiles at constant $x/c = 0.4, 0.5, 0.6, 0.7,$ and 0.8 at the phase 90°

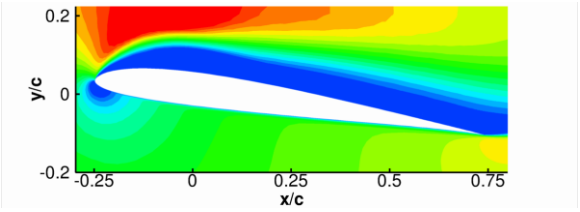

(b) u_1 contour at the phase 90°, CFD

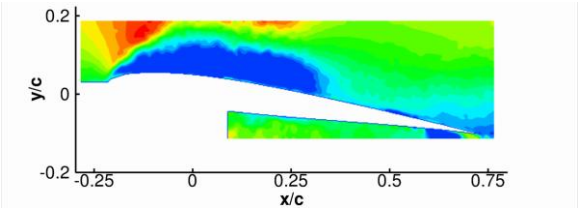

(c) u_1 contour at the phase 90°, PIV

Figure 15. u_1 profiles and contours from CFD and PIV results at Re = 3×10⁴ for the pure plunging case.

The results in Figure 15 show that the flow reattaches between 50% and 60% of the chord. The SST model predicts the velocity profile up to 50% of the chord, but it fails to capture the reattachment of the flow farther downstream. A similar trend was observed for Re = 6×10⁴ and is shown in Figure 16. A plausible explanation for these results is that the SST model[36,37] under predicts the eddy viscosity in the detached shear layer. Consequently, the momentum transfer towards the surface is reduced leading to an enlarged separated region in the flow[37].

Compared to Re = 3×10⁴ case, SST model predicted more attached flow compared to the experiments before the reattachment occurs. This could be due to increase in Re. In both cases, the velocity profile obtained from the experiments for the reattached flow differed greatly from the numerical data. Improvements need to be made to the numerical model in order to capture the reattachment flow accurately. Furthermore, the accuracy of the velocity profiles for the reattached flow should be another parameter of study.

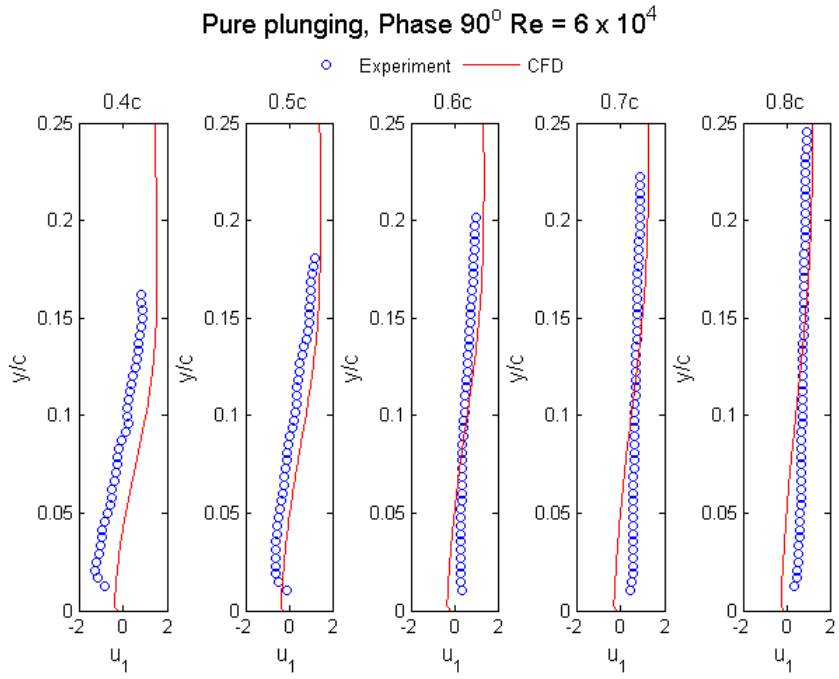

Figure 16. u_1 profiles at constant $x/c = 0.4, 0.5, 0.6, 0.7$ and 0.8 at the phase 90°at $Re = 6\times10^4$ for the pure plunging case.

IV. Summary and Conclusion

This paper considered a sequence of sinusoidal pitch and plunge of a SD7003 airfoil at three different Reynolds numbers with reduced frequency and Strouhal number kept constant at 0.25 and 0.08, respectively. In general, two-dimensional Reynolds-Averaged Navier-Stokes computations with the SST turbulence model gave qualitatively and quantitatively good comparison of velocity and vorticity fields compared to two-dimensional phase-averaged particle image velocimetry data in the water channel. For pitching and plunging case, the Reynolds number effect was minimal between $Re = 3\times10^4$ and $Re = 6\times10^4$; the flow was attached and the chordwise velocity profile showed excellent agreement between the experimental and the CFD data. At $Re = 1\times10^4$, flow separation was much stronger and experimental-computational agreement was degraded by the preponderance of large laminar regions. The resulting leading edge separation created a circulation zone and hence a leading edge vortex.

For pure plunging case, a large leading edge separation was observed for all Reynolds numbers considered. As the plunge motion progressed, the leading edge separation grew in size, decayed in strength and propagated downstream. The flow structure for the pure plunging case was similar between the experiments and the computation, except at phase 90° where computation predicted a tight trailing edge vortex, but phase-averaged PIV did not show a discernable TEV. At $Re = 3\times10^4$ and $Re = 6\times10^4$, a strong leading edge vortex was formed but the flow remained attached near the trailing edge. On the other hand, at $Re = 1\times10^4$, reattachment of the flow did not occur downstream of the LEV. The main difference between the two flows was the size of the leading edge vortex, which was larger at low Re. Such flow characteristic was not captured by the numerical simulation and the discrepancy was easily observed in the contour plots and velocity profiles.

The comparison between the lift coefficient from the numerical simulation and Theodorsen's prediction based on planar-wake model was in overall good qualitative agreement. In the pure plunging case, the positive lift increment due to LEV and decrement due to LEV convection downstream was not captured by the Theodorson model, but the discrepancy was localized to those phases of motion evincing these respective flowfield phenomena. The Theodorson prediction and the computed lift coefficient were essentially identical where the flow was nominally attached and near-wake nominally planar. This suggests that classical attached flow predictions for lift coefficient time-history remain useful, at least at the engineering level, even for cases with substantial flow separation.

In summary, Re effects were present for both pitching and plunging, and pure plunging cases. For pitching and plunging case, higher Re revealed more attached flow, whereas lower Re led to formation of a leading edge vortex. For pure plunging case, a leading edge separation was observed at all Re; however, higher Re caused the flow to form a strong leading edge vortex while showing attached flow downstream of the circulation zone. The discrepancies between the experiments and the computation at high Re arise from the fact that the SST turbulence model used in the computation was not able to capture the reattachment flow. The computed lift coefficient from CFD showed qualitative agreement with Theodorsen's prediction.

Acknowledgments

The work has been supported in part by the Air Force Office of Scientific Research's Multidisciplinary University Research Initiative (MURI) and by the Michigan/AFRL (Air Force Research Laboratory)/Boeing Collaborative Center in Aeronautical Sciences. We thank Dr. Hikaru Aono and Mr. Pat Trizila for the fruitful discussions provided.

References

[1] Shyy, W., Lian, Y., Tang, J., Viieru, D., and Liu, H. *Aerodynamics of Low Reynolds Number Flyers*. Cambridge University Press, 2008

[2] Sane, P.S., Dickinson, M.H., "The Control of Flight Force by a Flapping Wing: Lift and Drag Production," *Journal of Experimental Biology*, Vol. 204, 2001, pp. 2607–2626.

[3] Poelma, C., and Dickinson, M.H. "Time-Resolved Reconstruction of the Full Velocity Field around a Dynamically-Scaled Flapping Wing". Experiments in Fluids, Vol. 41, 2006, pp. 213-225.

[4] Shyy, W., Trizila, P., Kang, C., and Aono, H., "Can Tip Vortices Enhance Lift of a Flapping Wing?." *AIAA J.* (to be published)

[5] Usherwood, J.R. and Ellington, C.P. "The Aerodynamics of Revolving Wings I. Model Hawkmoth Wings*". Journal of Experimental Biology* Vol. 205, 2002, 1547–1564.

[6] Taylor, G. K., Nudds, R. L., and Thomas, A. L. R. Flying and swimming animals cruise at a Strouhal number tuned for high power efficiency, *Nature (London)* 425**,** 2003, 707–11.

[7] Tang, J., Viieru, D. and Shyy, W., "Effects of Reynolds Number and Flapping Kinematics on Hovering Aerodynamics," *AIAA J.*, Vol. 46, 2008, pp. 967-976.

[8] Trizila, P., Kang, C., Visbal, M.R. and Shyy, W., "Unsteady Fluid Physics and Surrogate Modeling of Low Reynolds Number, Flapping Airfoils," AIAA Paper No. 2008-3821, 38th AIAA Fluid Dynamics Conference and Exhibit, 2008.

[9] Shyy, W. and Liu, H., "Flapping Wings and Aerodynamic Lift: The Role of Leading-Edge Vortices," *AIAA J.*, Vol. 45, 2007, pp. 2817-2819.

[10] von Karman, T., and Sears, W. R., "Airfoil Theory for Nonuniform Motion," *Journal of the Aeronautical Sciences*, Vol. 5, No. 10, 1938, pp. 379–390

[11] Koochesfahani, M.M. "Vortical Patterns in the Wake of an Oscillating Airfoil," *AIAA J.* Vol. 27, No. 9, Sept. 1989, pp. 1200-1205.

[12] McCroskey, W. J., Carr, L. W., and McAlister, K. W., "Dynamic Stall Experiments on Oscillating Airfoils," *AIAA J.*, Vol. 14, No. 1., 1976, pp. 57-63.

[13] McCroskey, W. J., "Unsteady Airfoils," *Ann. Rev. Fluid Mech.*, Vol. 14, 1982, pp. 285-311.

[14] Carr, L., "Progress in Analysis and Prediction of Dynamic Stall," *J. Aircraft*, Vol., 25, 1988, pp. 6-17.

[15] Carr, L., and McCroskey, W. J., "A Review of Recent Advances in Computational and Experimental Analysis of Dynamic Stall," *IUTAM Symp. On Fluid Dynamics of High Angle of Attack*, 1992

[16] Ohmi, K., Coutanceau, M., Loc, T. P., and Dulieu, A., "Vortex Formation around an Oscillating and Translating Airfoil at Large Incidences," *J. Fluid Mech*., Vol. 211, 1990, pp. 37-60.

[17] Ohmi, K., Coutanceau, M., Daube, O., and Loc, T. P., "Further Experiments on Vortex Formation around an Oscillating and Translating Airfoil at Large Incidences," *J. Fluid Mech*., Vol. 225, 1991, pp. 607-630.

[18] Visbal, M., and Shang, J. S., "Investigation of the Flow Structure Around a Rapidly Pitching Airfoil," AIAA J., Vol. 27, No. 8, 1989, pp. 1044-1051.

[19] Choudhuri, G. P., and Knight, D. D., "Effects of Compressibility, Pitch Rate, and Reynolds Number on Unsteady Incipient Leading-edge Boundary Layer Separation over a Pitching Airfoil," *J. Fluid Mech*., Vol. 308, 1996, pp. 195-217.

[20] Platzer, M., and Jones, K. "Flapping Wing Aerodynamics - Progress and Challenges" AIAA-2006-500. Jan. 2006.

[21] Young, J., and Lai, J.C.S. "Oscillation Frequency and Amplitude Effects on the Wake of a Plunging Airfoil". *AIAA Journal*, Vol. 42, No. 10, 2004. pp. 2042-2052

[22] Lian, Y., and Shyy, W., "Aerodynamics of Low Reynolds Number Plunging Airfoil under Gusty Environment," AIAA Paper 2007-71, Reno, NV, 2007.
[23] Theodorsen, T., "General Theory of Aerodynamic Instability and the Mechanism of Flutter," *N.A.C.A. Report* 496, 1935
[24] OL, M.V. "Vortical Structures in High Frequency Pitch and Plunge at Low Reynolds Number". AIAA-2007-4233, 2007.
[25] Menter, F. R., "Zonal Two Equation k-ω Turbulence Models for Aerodynamic Flows," AIAA 93-2906
[26] Kamakoti, R., Thakur, S., Wright, J., and Shyy, W., "Validation of a new parallel all-speed CFD code in a rule-based framework for multidisciplinary applications", AIAA paper 2006-3063, June 2006.
[27] Shyy, W., "A Study of Finite Difference Approximations to Steady-State, Convection-Dominated Flow Problems", *Journal of Computational Physics*, Vol. 57, No. 3, 1985, pp. 415-438.
[28] Shyy, W., *Computational Modeling for Fluid Flow and Interfacial Transport*, Elsevier, Amsterdam, 1994.
[29] Thomas, P.D., and Lombard, K., "The Geometric Conservation Law – A Link between Finite-Difference and Finite-Volume Methods of Flow Computation on Moving Grids", AIAA 1978-1208, July 1978.
[30] Shyy, W., Udaykumar, H.S., Rao, M.M. and Smith, R.W. *Computational Fluid Dynamics with Moving Boundaries*, Taylor & Francis, Washington, DC, (1996, revised printing 1997, 1998 &2001); Dover, New York, 2007
[31] Sane, S.P., and Dickinson, M.H. "The Aerodynamic Effects of Wing Rotation and a Revised Quasi-Steady Model of Flapping Flight". *Journal of Experimental Biology*, Vol. 205, 2002, pp. 1087–1096.
[32] Leishman, J.G. *Principles of Helicopter Aerodynamics.* Cambridge University Press, 2000.
[33] Anderson, .J.M., Streitlien, K., Barrett, D.S., and Triantafyllou, M.S. "Oscillating Foils of High Propulsive Efficiency". *J. Fluid Mech.*, Vol. 360, 1998, pp. 41-72.
[34] Liiva, J. "Unsteady Aerodynamic and Stall Effects on Helicopter Rotor Blade Airfoil Sections". *J. Aircraft*, Vol. 6, No.1, 1969, pp. 46-51.
[35] Ol, M., McAuliffe, B. R., Hanff, E. S., Scholz, U., Kaehler, Ch., "Comparison of Laminar Separation Bubble Measurements on a Low Reynolds Number Airfoil in Three Facilities", AIAA 2005-5149, 2005.
[36] Menter, F.R., Kuntz, M., and Langtry, R., "Ten Years of Industrial Experience with the SST Turbulence Model," *Proc. Turbulence, Heat and Mass Transfer 4, eds.: Hanjalic, K., Nagano, Y., and Tummers, M.*, 2003
[37] Hutton, A.G., and Ashworth, R.M., "The Challenge of Turbulence Modelling in Modern Aeronautical Design," *Int. J. Numer. Meth. Fluids*, **47**, 2005, pp. 721-737